$$\int_{-s}^{s} \frac{\gamma_0(y_0)dy_0}{y-y_0} = 2\pi\alpha U \tag{10}$$

$$\int_{-s}^{s} \frac{\gamma_n(y_0)dy_0}{y-y_0} = -\sum_{m=0}^{n-1} K_m \int_{-s}^{s} (y-y_0)^n \gamma_{n-m-1}(y_0)dy_0$$

$$\equiv f_n(y) n \geq 1$$

Each of the $\gamma_n(y)$ has zero circulation, and the solution is (see Cheng and Rott[8])

$$\gamma_n(y) = \frac{1}{\pi^2}(s^2-y^2)^{-1/2}\int_{-s}^{s} \frac{f_n(y_0)(s^2-y_0^2)^{1/2}}{y_0-y}dy_0 \tag{11}$$

The singular integrals in Eqs. (10) and (11) are to be considered in the Cauchy principal value sense. Note that γ_0 is the solution due to R.T. Jones for $h\to\infty$ (see Plotkin[9]):

$$\gamma_0(y) = -2U\alpha y(s^2-y^2)^{-1/2} \tag{12}$$

Results and Discussion

Once $\gamma(y)$ is obtained, the jump in velocity potential across the wing surface can be found from an integration of

$$\phi_y(x,y,0\pm) = \pm\gamma(y)/2 \tag{13}$$

With the use of the linearized Bernoulli equation, the wing lift is given by[9]

$$L = \rho U\int_{-s}^{s} [\phi(c,y,0+)-\phi(c,y,0-)]dy \tag{14}$$

where ρ is the density. The nondimensional lift coefficient is

$$C_L \equiv 2L/\rho U^2 S \equiv C_{L\alpha}\alpha \tag{15}$$

where S is the planform area. Note that for $h\to\infty$ we get

$$(C_{L\alpha})_\infty = \pi A/2 \tag{16}$$

The lift curve slope for the slender wing in ground effect is

$$C_{L\alpha}/(C_{L\alpha})_\infty = 1+1/8(b/2H)^2-1/32(b/2H)^4$$

$$+0/(b/2H)^6] \tag{17}$$

where H is h at the wing trailing edge and additional terms can be obtained in a straightforward manner. Note that the result is independent of aspect ratio and is expected to be an increasingly accurate approximation as $A\to 0$.

To assess the validity of the slender-wing result, a widely used panel code[10] (VSAERO) was used to compute the lift coefficient for a delta wing in ground effect for values of aspect ratio less than one. (For thin wings, the method is the same as a quadrilateral vortex lattice method.) The method models the nonplanar trailing vortex sheet and allows for wake relaxation and rollup. Attached flow was assumed, and the angle of attack was 1 deg. The vortex lattice is formed by streamwise lines with cosine spacing along the span and radial lines from the tips with equal spacing along the chord. Forty panels along the chord and 10 panels along the semispan were used to deal with the small aspect ratios of interest.

Results of the computation for aspect ratios 1.0, 0.6, 0.2, and 0.05 are compared to the analytical result [Eq. (17)] in Fig. 1. It is seen that the computational results approach the analytical result as the aspect ratio approaches zero.

In conclusion, a closed-form solution is obtained for the increase in lift coefficient on a slender wing due to ground effect. The result is valid for low aspect ratios and moderate to large values of the ratio of trailing edge wall clearance to wing semispan.

References

[1]Katz, J., "Calculation of the Aerodynamic Forces on Automotive Lifting Surfaces," *Journal of Fluids Engineering*, Vol. 107, Dec. 1985, pp. 438–443.

[2]Deese, J.E. and Agarwal, R.K., "Euler Calculation for Flow Over a Wing in Ground Effect," AIAA Paper 86-1765 CP, 1986.

[3]Hashiguchi, M., Ohta, T., and Kuwahara, K., "Computational Study of Aerodynamic Behavior of a Car Configuration," AIAA Paper 87-1386, 1987.

[4]Tuck, E.O., "Steady Flow and Static Stability of Airfoils in Extreme Ground Effect," *Journal of Engineering Mathematics*, Vol. 15, 1981, pp. 89–102.

[5]Newman, J.N., "Analysis of Small-Aspect-Ratio Lifting Surfaces in Ground Effect," *Journal of Fluid Mechanics*, Vol. 117, 1982, pp. 305–314.

[6]Plotkin, A. and Kennell, C., "Thickness-Induced Lift on a Thin Airfoil in Ground Effect," *AIAA Journal*, Vol. 19, Nov. 1981, pp 1484–1486.

[7]Plotkin, A. and Tan, C.H., "Lifting-Line Solution for a Symmetrical Thin Wing in Ground Effect," *AIAA Journal*, Vol. 24, July 1986, pp. 1193–1194.

[8]Cheng, H.K., and Rott, N., "Generalizations of the Inversion Formula of the Thin Airfoil Theory," *Journal of Rational Mechanics and Analysis*, Vol. 3, 1954, pp. 357–382.

[9]Plotkin, A., "Thickness and Camber Effects in Slender Wing Theory," *AIAA Journal*, Vol. 21, Dec. 1983, pp. 1755–1757.

[10]Maskew, B., "Program VSAERO, A Computer Program for Calculating the Nonlinear Aerodynamic Characteristics of Arbitrary Configurations," NASA CR-166476, Nov. 1982.

Measurements of Turbulent Flow Behind a Wing-Body Junction

O. Özcan* and M. S. Ölçmen†
Istanbul Technical University, Istanbul, Turkey

Introduction

THE fluid mechanics problem of turbulent shear flow in the junction of a wing and aircraft fuselage is of significant practical and academic importance. The adverse pressure gradient caused by the wing leads to the separation of the boundary layer on the fuselage. A horseshoe vortex is formed in the separated flow region around the wing. Downstream of the wing and above the longitudinal horseshoe vortex, which is imbedded in the fuselage boundary layer, there is a shear-layer that is formed by the two merging boundary layers on the wing. The structure of the shear flow behind the wing is also influenced by the tip vortex, especially if the aspect ratio of the wing is small.

A limited amount of published experimental data exists for the wake of a wing-body junction. Nakayama and Rahai[1] report measurements in an idealized wing-body junction where both the wing and body are represented by flat surfaces and the wing is held at zero angle of attack. Velocity measurements in the wake of a wedge at zero angle of attack are described by Morrisette and Bushnell.[2] The present Note reports measurements in the turbulent shear flow behind a wing that is mounted on a flat plate at 30 deg of angle of attack. Various physical aspects of the flow are illuminated by the experimental data that include the skin-friction coefficient and pattern, the static pressure coefficient, and two mean velocity components. A detailed discussion of the experimental results is given in Özcan and Ölçemen.[3]

Received Jan. 22, 1987; revision received July 2, 1987.

*Assistant Professor, Faculty of Aeronautics and Astronautics.

†Graduate Student, Faculty of Aeronautics and Astronautics; currently at Virginia Polytechnic Institute and State University, Blacksburg, VA.

Experimental Conditions

The experiments were conducted in the 50 × 50-cm low-speed wind tunnel at Istanbul Technical Univ. The freestream velocity (U_∞), turbulence intensity and Reynolds number per unit length were 10 ± 0.3 (m/s), 0.4 ± 0.2 (%) and $(6.6 \pm 0.3)\ 10^5$ (1/m), respectively. A symmetrical, unswept and untwisted Joukowsky profile wing was used in the study. Figure 1 shows a schematic of the wing whose cord length, maximum thickness, and height were 128, 29, and 165 mm, respectively. The undisturbed boundary layer on the flat plate was turbulent and approximately 12 mm thick at the location of the wing leading-edge. Oil-flow visualization was made to observe the structure of the surface flowfield. A Preston-tube of 0.85 mm outer diameter was used to measure the shear-stress (τ_w) on the surface of the flat plate. The static pressure (p) on the flat plate was measured by a Furness Controls FC 001 micromanometer with an accuracy of ± 0.1 mm of water. A DISA 55M10 constant-temperature hot-wire anemometer was employed to measure the stream-wise and span-wise velocities (U and V) with an accuracy of ± 0.4 m/s.

Results and Conclusions

Figures 1 and 2 give the contour plots of the skin-friction coefficient $c_f = 2\tau_w/\rho_\infty U_\infty^2$ and the static pressure coefficient $c_p = 2(p_\infty - p)/\rho_\infty U_\infty^2$ on the flat plate. p_∞ and ρ_∞ are the freestream pressure and density, respectively. The dotted lines show the extrapolated parts of the contours in flow regions where data are not available. The thin broken lines denote the separation and reattachment lines that are discussed in the next paragraph. The contour plots reveal a characteristic W-shaped

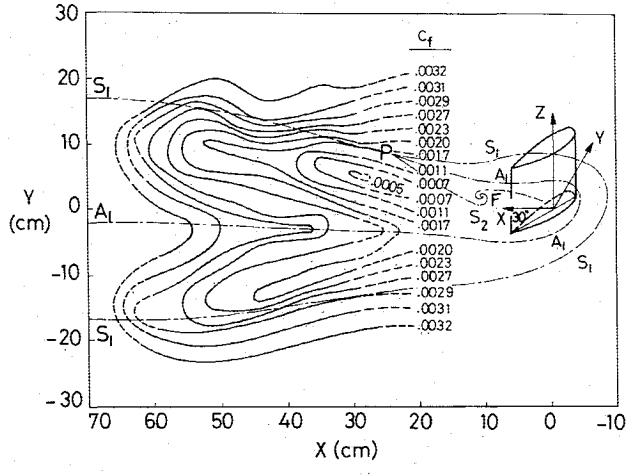

Fig. 1 Schematic of model and contour plot of skin-friction coefficient $c_f = 2\tau_w/\rho_\infty U_\infty^2$.

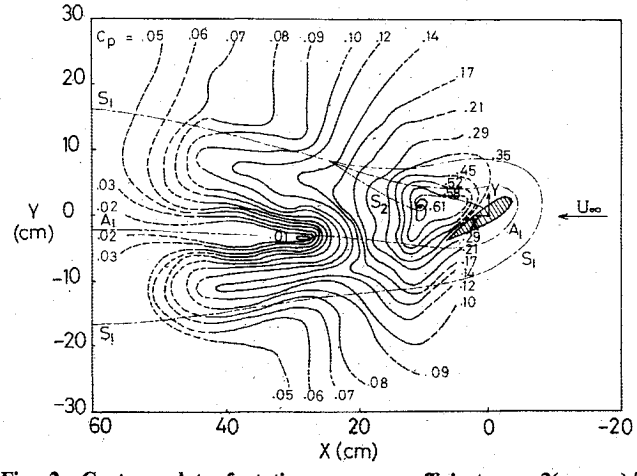

Fig. 2 Contour plot of static pressure coefficient $c_p = 2(p_\infty - p)/\rho_\infty U_\infty^2$.

footprint of the horseshoe vortex. Sufficiently downstream of the wing the span-wise variation of c_f shows a valley, a peak, and another valley, whereas the span-wise variation of c_p reveals a peak, a valley, and another peak. The valley between the two peaks disappears in the span-wise variation of c_p for $X < 20$ cm. The distances between the Y locations of the peaks and valleys indicate that the $Y < 0$ leg of the horseshoe vortex is smaller than the $Y > 0$ leg. The differences between the magnitudes of the peaks and valleys are larger for the $Y > 0$ leg than the $Y < 0$ leg. This indicates that the $Y > 0$ leg of the horseshoe vortex is stronger (has more circulation) than the leg located in the $Y < 0$ region.

The thin broken lines in Figs. 1 and 2 denote the separation and reattachment lines measured from the observed oil-flow pattern. In addition to a U-shaped separation line (S_1) where the horseshoe vortex sheds, there is a secondary separation line (S_2) that originates from the wing and joins S_1 at point P. The reattachment line A_1, which originates from a node ahead of the wing, also joins S_1 at point P. A tornado vortex is located at point F above the surface. The counter-clockwise rotating tornado vortex rises vertically from the surface above the turbulent boundary layer before it bends downstream and becomes a longitudinal vortex. The base of the tornado vortex coincides with the minimum pressure (maximum c_p) region on the flat plate.

The shape of the reattachment line A_1 indicates that the $Y > 0$ leg of the horseshoe vortex is fed by the severely decelerated fluid behind the wing. On the other hand, the $Y < 0$ leg of the horseshoe vortex does not encounter the minimum pressure region behind the wing as it comes from the wing windward side. The secondary separation line S_2 is located in the adverse pressure gradient region behind the wing. The fact that c_f values are smaller in the $Y > 0$ region than in the $Y < 0$ region is also an indication of a more severely retarded flow in the $Y > 0$ region. It appears that the $Y < 0$ leg of the horseshoe vortex moves faster than the $Y > 0$ leg in the stream-wise direction. As the horseshoe vortex transports momentum towards the reattachment line, boundary-layer thickness decreases and momentum transfer increases. Consequently, the locations of maximum c_f are located along the reattachment line as revealed by Fig. 1.

Figure 3 gives a postulated quasisteady streamline pattern in the cross-flow plane at $X = 29.5$ cm. The dotted lines show the

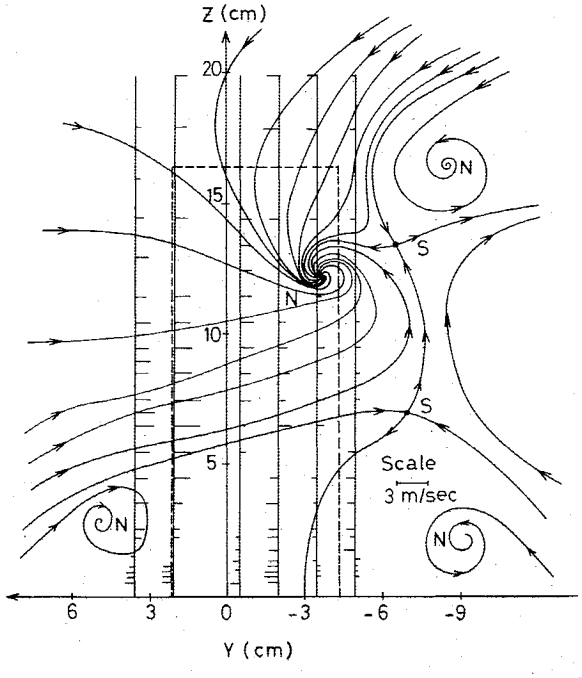

Fig. 3 Vertical variation of span-wise velocity V for $Y = 3.5$, 2, -0.5, -2, -3.5, and -5 cm at $X = 29.5$ cm.

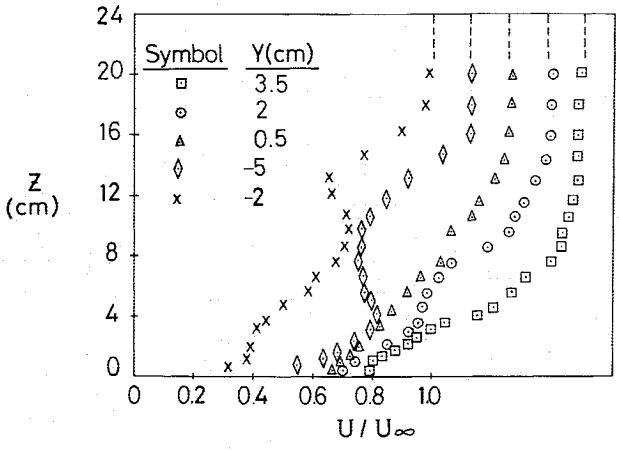

Fig. 4 Vertical variation of normalized stream-wise velocity U/U_∞ for $Y = 3.5, 2, 0.5, -2$, and -5 cm at $X = 29.5$ cm.

projection of the wing on the plane of the figure. The saddle and nodal-type singular points in the streamline pattern are denoted by letters S and N, respectively. The horizontal line elements attached to the $Y =$ constant lines show both the magnitude and direction of the span-wise velocity (V) measured at this particular X location. The velocity data support the validity of the hypothesized streamline pattern. The tip vortex is located at a higher Z location than the tornado vortex. The tip and tornado vortices are deflected in the negative Y direction as they move downstream. This is probably due to the inviscid turning of the freestream by the wing in the negative Y direction. The large negative V velocities in the $Y > 0$ region away from the flat plate also indicate such an inviscid flow deflection. The span-wise velocities given in Fig. 3 confirm that the $Y > 0$ leg of the horseshoe vortex is larger and stronger than the $Y < 0$ leg.

Figure 4 gives the vertical variation of the normalized stream-wise velocity U/U_∞ for various Y locations at $X = 29.5$ cm. The origin of the plot is displaced to the right by 0.125 for each of the Y stations. The location of $U/U_\infty = 1$ for each profile is denoted by dotted lines. Figure 4 shows that the normalized stream-wise velocity U/U_∞ increases monotonically with increasing Z in the $Y > 0$ region, whereas the stream-wise velocity profiles in the $Y < 0$ region exhibit S-shaped variations in the Z direction. It appears that the tip vortex and the tornado vortex that are both located in the $Y < 0$ region are responsible for the S-shaped profiles. Trentacosta and Sforza[4] report irregularities in stream-wise velocity profiles around the potential cores of three-dimensional jets. They suggest that the irregularities are generated by the induced velocities of a decaying vortex ring surrounding the jet. It may be argued that as the longitudinal tip and tornado vortices are deflected in the negative Y direction, they become capable of inducing a stream-wise velocity component in the surrounding fluid and, thus, generate the S-shaped profiles. A vortical flow structure similar to the Karman vortex street can also be responsible for the generation of S-shaped profiles. Morrisette and Bushnell[2] also observe irregular-shaped stream-wise velocity profiles in the wake of a wedge at zero angle of attack. They report that longitudinal vortices, which originate from the vicinity of the wake neck, are the cause of large deficits in the streamwise velocity. Morrisette and Bushnell[2] hypothesize that the concave curvature of the shear layer approaching the wake neck leads to the generation of Taylor-Gortler vortices. Further experimental work is needed to check the existence of Taylor-Gortler-type vortices in the flow of the present study. Conversely, one may hypothesize that the vortices observed in Ref. 2 are a pair of tornado vortices that are fed by the flow separated from both two sides of the wedge. Tani et al.[5] observe two counter-rotating tornado vortices behind a cylinder mounted on a plate. Any evidence of a second tornado vortex could not be observed in the present study. This was probably due to the attached flow conditions on the windward side of the wing where flow separation from the trailing edge did not lead to a sufficiently large reversed-flow region.

References

[1]Nakayama, A. and Rahai, H. R., "Measurements of Turbulent Flow Behind a Flat Plate Mounted Normal to the Wall," *AIAA Journal*, Vol. 22, Dec. 1984, pp. 1817–1819.

[2]Morrisette, E. L. and Bushnell, D. M., "Evidence of Imbedded Vortices in a Three-Dimensional Shear Flow," *AIAA Journal*, Vol. 19, March 1981, pp. 400–402.

[3]Özcan, O. and Ölçmen, M. S., "Measurements of Turbulent Flow Behind a Wing-Body Junction," *Proceedings of the Sixth Symposium on Turbulent Shear Flows*, Toulouse, France, Sept. 1987.

[4]Trentacosa, N. and Sforza, P., "Further Experimental Results for Three-Dimensional Free Jets," *AIAA Journal*, Vol. 5, May 1967, pp. 885–891.

[5]Tani, I., Komoda, H., Komatsu, Y., and Iuchi, M., "Boundary-Layer Transition by Isolated Roughness," Rept. No. 375, Aeronautical Research Inst., Univ. of Tokyo, Nov. 1962.

Turbulent Viscous Drag Reduction with Thin-Element Riblets

B. Lazos* and S. P. Wilkinson*
NASA Langley Research Center, Hampton, Virginia

Introduction

THE parametric studies by Walsh and Lindemann[1] of various riblet geometries established the symmetric V-groove riblet as a practical means for turbulent viscous drag reduction. In an effort to improve riblet performance, an experimental program was initiated to extend the riblet data base to additional, untested riblet geometries. One achievement of this program was the identification of the thin-element, rectangular geometry with a maximum drag reduction equal to the symmetric V-groove (8%) and drag reduction at larger riblet spacings.

The current geometry consists of very thin ribs extending perpendicularly from the wall and aligned in the streamwise direction. They form an array of streamwise channels in the near-wall region whose height and spacing may be varied independently without affecting the spanwise contour of the region between adjacent riblets. Independent height and spacing control is a particularly desirable feature for proper parametric study. This geometry was selected for direct drag study primarily because of turbulence intensity data obtained for similar models in a previous study,[2] which showed a significant impact of the thin-element design on the intensity level and distribution.

Model Construction and Apparatus

Thin-Element riblet model construction is illustrated in Fig. 1a. As shown, thin metal strips were clamped between spacers defining the channel height and width. The metal strips had sharp, square edges and were 0.002 in. thick (approximately 1–2 viscous wall lengths). A more practical model in terms of potential application with a similar geometry was also tested and consisted of adjacent trapezoidal elements formed in con-

Received April 9, 1987; revision received June 1, 1987.

*Aerospace Engineer, Viscous Flow Branch, High-Speed Aerodynamics Division. Member AIAA.